

# DM-NeRF: 3D Scene Geometry Decomposition and Manipulation from 2D Images

Bing Wang<sup>1,2†</sup>, Lu Chen<sup>1†</sup>, Bo Yang<sup>1\*</sup>

<sup>1</sup>vLAR Group, The Hong Kong Polytechnic University   <sup>2</sup> University of Oxford  
bing.wang@cs.ox.ac.uk   lu.chen@polyu.edu.hk   bo.yang@polyu.edu.hk

**Abstract.** In this paper, we study the problem of 3D scene geometry decomposition and manipulation from 2D views. By leveraging the recent implicit neural representation techniques, particularly the appealing neural radiance fields, we introduce an object field component to learn unique codes for all individual objects in 3D space only from 2D supervision. The key to this component is a series of carefully designed loss functions to enable every 3D point, especially in non-occupied space, to be effectively optimized even without 3D labels. In addition, we introduce an inverse query algorithm to freely manipulate any specified 3D object shape in the learned scene representation. Notably, our manipulation algorithm can explicitly tackle key issues such as object collisions and visual occlusions. Our method, called DM-NeRF, is among the first to simultaneously reconstruct, decompose, manipulate and render complex 3D scenes in a single pipeline. Extensive experiments on three datasets clearly show that our method can accurately decompose all 3D objects from 2D views, allowing any interested object to be freely manipulated in 3D space such as translation, rotation, size adjustment, and deformation.

**Keywords:** 3D Scene Decomposition, 3D Scene Manipulation

## 1 Introduction

In many cutting-edge applications such as mixed reality on mobile devices, users may desire to virtually manipulate objects in 3D scenes, such as moving a chair or making a flying broomstick in a 3D room. This would allow users to easily edit real scenes at fingertips and view objects from new perspectives. However, this is particularly challenging as it involves 3D scene reconstruction, decomposition, manipulation, and photorealistic rendering in a single framework [30].

A traditional pipeline firstly reconstruct explicit 3D structures such as point clouds or polygonal meshes using SfM/SLAM techniques [27,4], and then identify 3D objects followed by manual editing. However, these explicit 3D representations inherently discretize continuous surfaces, and changing the shapes often requires additional repair procedures such as remeshing [2]. Such discretized and manipulated 3D structures can hardly retain geometric details with appearance, resulting in the generated novel views to be unappealing. Given this, it is worthwhile to design a new pipeline which can recover continuous 3D scene geometry only from 2D views and enable object decomposition and manipulation.

\* Corresponding Author, † Equal Contribution

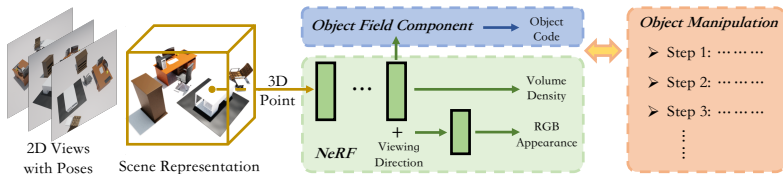


**Fig. 1.** The general workflow and components of our framework. The existing NeRF is used as our backbone shown by the green block, and we propose the object field and manipulation components shown by the blue and orange blocks.

Recently, implicit representations, especially NeRF [21], emerge as a promising tool to represent continuous 3D geometries from images. A series of succeeding methods [3,5,47] are rapidly developed to decouple lighting factors from structures, allowing free edits of illumination and materials. However, these methods fail to decompose the 3D scene geometry into individual objects. Therefore, it is not possible to manipulate individual object shapes in complex scenes. A handful of recent works [33,46] have started to learn disentangled shape representations for potential geometry manipulation. However, they either focus on single objects or simple synthetic scenes, and can hardly extend to real-world 3D scenes with dozens of objects and severe visual occlusions. Another two recent works [42,26] address the similar task as ours. However, the work [42] only decomposes a foreground object instead of segmenting every object, while the work [26] focuses on decomposing dynamic objects.

In this paper, we aim to design a new method to simultaneously recover continuous 3D scene geometry, segment all individual objects in 3D space, and support flexible object shape manipulation such as translation, rotation, size adjustment and deformation. In addition, the edited 3D scenes can be also rendered from novel views. However, this task is extremely challenging as it requires: 1) an object decomposition approach amenable to continuous and implicit 3D fields, without relying on any 3D labels for supervision due to the infeasibility of collecting labels in continuous 3D space; 2) an object manipulation method agreeable to the learned implicit and decomposed fields, with a ability to clearly address visual occlusions inevitably caused by manipulation.

To tackle these challenges, we introduce a simple pipeline, called **DM-NeRF**, which is built on the successful NeRF, but able to **d**ecompose the entire 3D space into object fields and freely **m**anipulate their geometries for realistic novel view rendering. As shown in Figure 1, our method consists of three major components: 1) the existing radiance fields as backbone to learn volume density and appearance for every 3D point in space; 2) the object field which learns a unique object code for every 3D point; 3) the object manipulator which directly edits the shape of any specified object and automatically tackles visual occlusions.

The **object field** is the core of our framework. This component aims to predict a unique one-hot vector, *i.e.*, object code, for every 3D point in the entire scene space. However, to learn such code involves critical issues: 1) there are no ground truth 3D object codes available for full supervision; 2) the number of total objects is variable and there is no fixed order for objects; 3) the non-occupied (empty) 3D space must be taken into account, but there are no labels

for supervision as well. As detailed in Section 3.2, we show that our object field together with a series of carefully designed loss functions can address them properly, under the supervision of color images with object 2D masks only.

Once the object field is well learned, our **object manipulator** aims to directly edit the geometry and render novel views when specifying the target objects, viewing angles, and manipulation settings. A naïve method is to obtain explicit 3D structures followed by manual editing and rendering, so that any shape occlusion and collision can be explicitly addressed. However, it is extremely inefficient to evaluate dense 3D points from implicit fields. To this end, as detailed in Section 3.3, we introduce a lightweight inverse query algorithm to automatically edit the scene geometry and appearance.

Overall, our pipeline can simultaneously recover 3D scene geometry, decompose and manipulate object instances only from 2D images. Extensive experiments on multiple datasets demonstrate that our method can precisely segment all 3D objects and effectively edit 3D scene geometry, without sacrificing high fidelity of novel view rendering. Our key contributions are:

- We propose an object field to learn a unique code for all 3D objects and non-occupied space only from 2D images.
- We propose an inverse query algorithm to effectively edit specified object shapes, while generating realistic scene images from novel views.
- We demonstrate superior performance for 3D decomposition and manipulation, and also contribute the first synthetic dataset for quantitative evaluation of 3D scene editing. Our data and code are available at: <https://github.com/vLAR-group/DM-NeRF>

## 2 Related Work

**Explicit 3D Representations:** To represent 3D geometry of objects and scenes from images or point clouds, voxel grids [7], octree [35], triangle meshes [16,12], point clouds [10] and shape primitives [50] are widely used. Although impressive progress has been achieved in shape reconstruction [43,41], completion [32], shape generation [18], and scene understanding [38,11], the quality of these discrete shape representations are inherently limited by the spatial resolution and memory footprint. Therefore, they are hard to represent complex 3D scenes.

**Implicit 3D Representations:** To overcome the discretization issue of explicit representations, coordinate based MLPs have been recently proposed to learn implicit functions to represent continuous 3D shapes. These implicit representations can be generally categorized as: 1) signed distance fields [28], 2) occupancy fields [20], 3) unsigned distance fields [6,39], 4) radiance fields [21], and 5) hybrid fields [40]. Among them, both occupancy fields and signed distance fields can only recover closed 3D shapes, and is hard to represent open scene geometries. In the past two years, these representations have been extensively studied for novel view synthesis [25,37] and 3D scene understanding [45,48]. Thanks to the powerful representation capability, impressive results have been achieved, especially the neural radiance fields and its succeeding methods. In this paper, we also leverage the success of implicit representations, particularly NeRF, to recover the geometry and appearance of 3D scenes from 2D images.

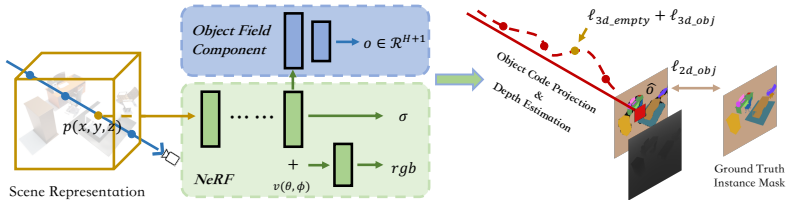


**Fig. 2.** The architecture of our pipeline. Given a 3D point  $\mathbf{p}$ , we learn an object code through a series of loss functions using both 2D and 3D supervision signals.

**3D Object Segmentation:** To identify 3D objects from complex scenes, existing methods generally include 1) image based 3D object detection [22], 2) 3D voxel based detection methods [49] and 3) 3D point cloud based object segmentation methods [44]. Given large-scale datasets with full 3D object annotations, these approaches have achieved excellent object segmentation accuracy. However, they are designed to process explicit and discrete 3D geometries. Therefore, they are unable to segment continuous and fine-grained shapes, and fail to support geometry manipulation and realistic rendering. With the fast development of implicit representation of 3D scenes, it is desirable to learn object segmentation for implicit surfaces. To the best of our knowledge, this paper is among the first to segment all 3D objects of implicit representations for complex scenes, only with color images and 2D object labels for supervision.

**3D Scene Editing:** To edit 3D scenes from images, existing methods can be categorized as 1) appearance editing and 2) shape editing. A majority of works [31,3,47,5] focus on lighting factor decomposition for appearance editing. Although achieving appealing results, these approaches cannot separately manipulate individual objects. A number of recent works [23,19,15,33,13] start to learn disentangled shape representations for potential geometry manipulation. However, they can only deal with single objects or simple scenes, without being able to learn unique object codes for precise shape manipulation and novel view rendering. In addition, there are also a plethora of works [36,24,9,1] on generation based scene editing. Although they can manipulate the synthesized objects and scenes, they cannot discover and edit objects from real-world images.

## 3 DM-NeRF

### 3.1 Overview

Given a set of  $L$  images for a static scene with known camera poses and intrinsics  $\{(\mathcal{I}_1, \boldsymbol{\xi}_1, \mathbf{K}_1) \cdots (\mathcal{I}_L, \boldsymbol{\xi}_L, \mathbf{K}_L)\}$ , NeRF [21] uses simple MLPs to learn the continuous 3D scene geometry and appearance. In particular, it takes 5D vectors of query point coordinates  $\mathbf{p} = (x, y, z)$  and viewing directions  $\mathbf{v} = (\theta, \phi)$  as input, and predicts the volume density  $\sigma$  and color  $\mathbf{c} = (r, g, b)$  for point  $\mathbf{p}$ . In our pipeline, we leverage this vanilla NeRF as the backbone to learn the continuous scene representations, although other NeRF variants can also be used. Our method aims to decompose all individual 3D objects, and freely manipulate any object in the 3D scene space. To achieve this, we design an object field component to parallelly learn a unique object code for every query point  $\mathbf{p}$ , together with a object manipulator to edit the learned radiance fields and object fields.

### 3.2 Object Fields

**Object Field Representation:** As shown in Figure 2, given the input point  $\mathbf{p}$ , we model the object field as a function of its coordinates, because the object signature of a 3D point is irrelevant to the viewing angles. The object field is represented by a one-hot vector  $\mathbf{o}$ . Basically, this one-hot object code aims to accurately describe the object ownership of any point in 3D space.

However, there are two issues involved here: 1) the total number of objects in 3D scenes are variable and it can be 1 or many; 2) the entire 3D space has a large non-occupied volume in addition to solid objects. To tackle these issues, we define the object code  $\mathbf{o}$  as  $H + 1$  dimensional, where  $H$  is a predefined number of solid objects that the network are expected to predict in maximum. We can safely choose a relative large value for  $H$  in practice. The last dimension of  $\mathbf{o}$  is particularly reserved to represent the non-occupied space. Notably, this careful design is crucial for tackling occlusion and collision during object manipulation discussed in Section 3.3. Formally, the object field is defined as:

$$\mathbf{o} = f(\mathbf{p}), \quad \text{where } \mathbf{o} \in \mathcal{R}^{H+1} \quad (1)$$

The function  $f$  is parameterized by a series of MLPs. If the last dimension of code  $\mathbf{o}$  is 1, it represents the input point  $\mathbf{p}$  is non-occupied or the point is empty.

**Object Code Projection:** Considering that it is infeasible to collect object code labels in continuous 3D space for full supervision while it is fairly easy and low-cost to collect object labels on 2D images, we aim to project the object codes along the query light ray back to a 2D pixel. Since the volume density  $\sigma$  learned by the backbone NeRF represents the geometry distribution, we simply approximate the projected object code of a pixel  $\hat{\mathbf{o}}$  using the sampling strategy and volume rendering formulation of NeRF. Formally, it is defined as:

$$\hat{\mathbf{o}} = \sum_{k=1}^K T_k \alpha_k \mathbf{o}_k, \quad \text{where } T_k = \exp(-\sum_{i=1}^{k-1} \sigma_i \delta_i), \quad \alpha_k = 1 - \exp(-\sigma_k \delta_k) \quad (2)$$

with  $K$  representing the total sample points along the light ray shooting from a pixel,  $\sigma_i$  representing the learned density of the  $i^{\text{th}}$  sample point,  $\delta_k$  representing the distance between the  $(k + 1)^{\text{th}}$  and  $k^{\text{th}}$  sample points. From this projection formulation, we can easily obtain 2D masks of 3D object codes given the pose and camera parameters of any query viewing angles.

**Object Code Supervision:** Having the projected 2D object predictions at hand, we naturally choose 2D images with object annotations for supervision. However, there are two issues: 1) The number and order of ground truth objects can be very different across different views due to visual occlusions. For example, as to the same 3D object in space, its object annotation in image #1 can be quite different from its annotation in image #2. Therefore, it is non-trivial to correctly and consistently utilize 2D object annotations to supervise the network. 2) The 2D object annotations can only provide labels for 3D solid objects, because the non-occupied 3D space will never be recorded in 2D images. Therefore, it is impossible to directly supervise the non-occupied space, *i.e.*, the last dimension of  $\hat{\mathbf{o}}$ , from 2D annotations. Due to these issues, to simply borrow existing 2D object segmentation methods such as MaskRCNN [14] is ineffective, because they fundamentally do not consider the consistency between 3D and 2D.

To tackle the first issue, we use the Optimal Association and Supervision strategy proposed by 3D-BoNet [44]. As illustrated in Figure 3, assuming we generate  $L$  images of 2D object predictions and have the paired  $L$  images of 2D ground truth object labels, in every single image, we use Hungarian algorithm [17] to associate every ground truth 2D object mask with a unique predicted 2D object mask according to two criteria, Soft Intersection-over-Union (sIoU) and Cross-Entropy Score (CES) [44]. Once the predicted and ground truth 2D objects are matched, we directly maximize the average sIoU score and minimize the CES across all  $L$  images. Formally, the loss is defined as follows. Details of the calculation and matching are in appendix.

$$\ell_{2d.obj} = \sum_{l=0}^L (-sIoU_l + CES_l) \quad (3)$$

Noted that, we only use the first  $H$  object predictions in every image to match with ground truth 2D objects because these are the solid objects, while the last dimension of  $\hat{o}$  is never used at this stage. After all, our optimal association strategy explicitly takes into account the consistency across all images from different viewing angles, driving the network to automatically learn a unique code for all 3D solid objects from only 2D labels.

To tackle the second issue, we turn to supervise the non-occupied object code in 3D space with the aid of estimated surface distances. In particular, given a specific query light ray on which we sample  $K$  3D points to compute the projected 2D object code  $\hat{o}$ , we simultaneously compute an approximate distance  $d$  between the surface and camera center along that query light:

$$d = \sum_{k=1}^K T_k \alpha_k \delta_k, \quad \text{where} \quad T_k = \exp\left(-\sum_{i=1}^{k-1} \sigma_i \delta_i\right), \quad \alpha_k = 1 - \exp(-\sigma_k \delta_k) \quad (4)$$

As illustrated in Figure 4, once we have the surface distance  $d$  at hand, we can easily know the relative position between every sample point  $k$  and the surface point  $s$  along the light ray. Naturally, we can then identify the subset of sample points surely belonging to empty space as indicated by green points, the subset of sample points near the surface as indicated by red points, and the remaining subset of sample points behind the surface as indicated by black points. Such geometric information provides critical signals to supervise empty space, *i.e.*, the last dimension of object code  $\mathbf{o}$ . Note that, the sample points behind the surface may not surely belong to empty space, and therefore we should not use them as supervision signals. Mathematically, we use the following kernel functions to obtain a surfaceness score  $s_k$  and an emptiness score  $e_k$  for the  $k^{th}$  sample point with the indicator function represented by  $\mathbb{1}()$ .

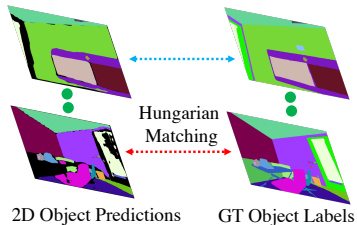


Fig. 3. Illustration of 2D object matching and supervision.

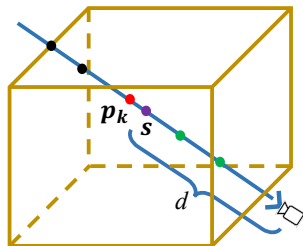


Fig. 4. Empty points identification from estimated surface distance.

$$s_k = \exp(-(d_k - d)^2) \quad e_k = (1 - s_k) * \mathbb{1}(d - \Delta d - d_k > 0) \quad (5)$$

where  $d_k$  represents the distance between camera center and the  $k^{th}$  sample point, and  $\Delta d$  is a hyperparameter to compensate the inaccuracy of estimated surface distance  $d$ . Note that, the indicator function is used to mask out the sample points behind surface point during loss calculation. Given the emptiness and surfaceness scores for the total  $K$  sample points along the ray, we use the simple log loss to supervise the last dimension of object code denoted as  $o_k^{H+1}$ .

$$\ell_{3d\_empty} = -\frac{1}{K} \sum_{k=1}^K \left( e_k * \log(o_k^{H+1}) + s_k * \log(1 - o_k^{H+1}) \right) \quad (6)$$

Since there should be no solid object at all in the empty space, we apply the following loss on the first  $H$  dimensions of the object code to push them to be zeros. The  $h^{th}$  dimension of the  $k^{th}$  sample point’s object code is denoted by  $o_k^h$ .

$$\ell_{3d\_obj} = -\frac{1}{K} \sum_{k=1}^K \left( e_k * \sum_{h=1}^H \log(1 - o_k^h) \right) \quad (7)$$

To sum up, we firstly project object codes in 3D space back to 2D pixels along light rays using volume rendering equation, and then use optimal association strategy to compute the loss value with 2D object labels only. In addition, we introduce the key emptiness and surfaceness scores for points in 3D space with the aid of estimated surface distances. These unique scores are used to supervise the non-occupied 3D space. The whole object field is jointly supervised by:

$$\ell = \ell_{2d\_obj} + \ell_{3d\_empty} + \ell_{3d\_obj} \quad (8)$$

### 3.3 Object Manipulator

If we want to manipulate a specific 3D object shape such as translation, rotation and size adjustment, how does the whole scene look like in a new perspective after our manipulation? assuming that the object code and manipulation matrix can be precomputed from the users’ interaction such as click, drag or zoom.

Intuitively, there could be two strategies: 1) Firstly project 3D scene into 2D images, and then edit objects in 2D space. 2) Firstly edit objects in 3D space, and then project into 2D images. Compared with the first strategy which would inevitably incur inconsistency across multiple images due to the independent edits on individual views, the latter is more favourable. Remarkably, our object field component can support the latter manipulation strategy. Regarding such a manipulation task on implicit fields, the core question is: how do we edit the codes  $\sigma/c/o$  of every sample point along the query light ray, such that the generated novel view exactly shows the new appearance? This is nontrivial as:

- First, we need to address potential collisions between objects during manipulation. In fact, this is quite intuitive, thanks to our special design of the emptiness score in the last dimension of object code  $o$ .
- Second, due to visual occlusions, the object codes behind surface points may not be accurate because they are not sufficiently optimized. By comparison, the projected object code  $\hat{o}$  along a light ray tends to be more accurate primarily because we have ground truth 2D labels for strong supervision.
- At last, we need a systematic procedure to update the codes with the known manipulation information. To this end, we design an inverse query approach.

**Inverse Query:** Here, we introduce a creative inverse query approach to address all above issues, realizing the favourable strategy: *editing in 3D space followed by 2D projection*. In particular, as illustrated in Figure 5, for any 3D sample point  $\mathbf{p}_k$  along a specific query light ray, given the *target* (i.e., to-be-edited) object code  $\mathbf{o}_t$  and its manipulation settings: relative translation  $\Delta\mathbf{p} = (\Delta x, \Delta y, \Delta z)$ , rotation matrix  $\mathbf{R}^{3 \times 3}$ , and scaling factor  $t > 0$ , we firstly compute an inverse 3D point  $\mathbf{p}_{k'}$ , and then evaluate whether  $\mathbf{p}_k$  and  $\mathbf{p}_{k'}$  belong to the target object, and lastly decide to whether edit the codes or not. Formally, we introduce Inverse Query Algorithm 1 to conduct a single light ray editing and rendering for object shape manipulation. Naturally, we can shoot a bunch of rays from any novel viewing angles to generate images of manipulated 3D scenes.

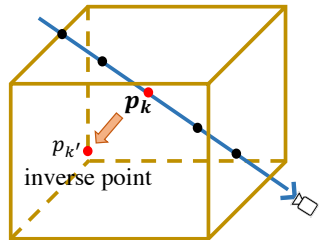


**Fig. 5.** An illustration of computing inverse points.

### 3.4 Implementation

To preserve the high-quality of image rendering, our loss in Equation 8 is only used to optimize the MLPs of object field branch. The backbone is only optimized by the original NeRF photo-metric loss [21]. The whole network is end-to-end trained from scratch. The single hyper-parameter for our object field  $\Delta d$  is set as 0.05 meters in all experiments. All other implementation details are in appendix.

## 4 Experiments

### 4.1 Datasets

**DM-SR:** To the best of our knowledge, there is no existing 3D scene dataset suitable for quantitatively evaluation of geometry manipulation. Therefore, we create a synthetic dataset with 8 types of different and complex indoor rooms, called DM-SR. The room types and designs follow Hypersim dataset [29]. Each scene has a physical size of about  $12 \times 12 \times 3$  meters with around 8 objects. We generate the following 5 groups of images.

- Group 1 (Before Manipulation): Each scene is rendered with color images and 2D object masks at  $400 \times 400$  pixels from viewpoints sampled on the upper hemisphere. Each scene generates 300 views for training and 100 for testing. The rendering trajectories follow NeRF synthetic dataset [21].
- Group 2 (Translation Only): One object in each scene is picked up to be translated along  $X$  or  $Y$  axis with about 0.3 meter. Then 100 views are generated for testing at the same testing viewpoints in Group 1.
- Group 3 (Rotation Only): One object in each scene is picked up to be rotated around  $z$  axis with about 90 degrees. Then 100 views are generated for testing at the same testing viewpoints in Group 1.
- Group 4 (Scaling Only): One object in each scene is picked up to be scaled down about  $0.8 \times$  smaller. Then 100 views are generated for testing at the same testing viewpoints in Group 1.



---

**Algorithm 1** Our Inverse Query Algorithm to manipulate the learned implicit fields. (1)  $\mathbf{o}_t$  is the target object code, one-hot with  $H + 1$  dimensions.  $\{\Delta\mathbf{p}, \mathbf{R}^{3 \times 3}, t > 0\}$  represent the manipulation information for the target object. (2)  $\{\mathbf{p}_1 \cdots \mathbf{p}_k \cdots \mathbf{p}_K\}$  represent the  $K$  sample points along a specific query light ray  $\mathbf{r}$ . Note that, we convert all object codes into hard one-hot vectors for easy implementation.

---

**Input:**

- The target object code  $\mathbf{o}_t$ , manipulation information  $\{\Delta\mathbf{p}, \mathbf{R}^{3 \times 3}, t \geq 0\}$ ;
- The sample points  $\{\mathbf{p}_1 \cdots \mathbf{p}_k \cdots \mathbf{p}_K\}$  along a specific query light ray  $\mathbf{r}$ ;

**Output:**

- The final pixel color  $\bar{\mathbf{c}}$  rendered from the query ray  $\mathbf{r}$  after manipulation;
- The final pixel object code  $\bar{\mathbf{o}}$  rendered from the query ray  $\mathbf{r}$  after manipulation;

**Preliminary step:**

- Obtain the projected pixel object code  $\hat{\mathbf{o}}$  of light ray  $\mathbf{r}$  before manipulation;

*NOTE: The loop below shows how to edit per sample point in 3D space.*

**for**  $\mathbf{p}_k$  in  $\{\mathbf{p}_1 \cdots \mathbf{p}_k \cdots \mathbf{p}_K\}$  **do**

- Compute the inverse point  $\mathbf{p}_{k'}$  for  $\mathbf{p}_k$ :  $\mathbf{p}_{k'} = (1/t)\mathbf{R}^{-1}(\mathbf{p}_k - \Delta\mathbf{p})$ ;
- Obtain the codes  $\{\sigma_k, \mathbf{c}_k, \mathbf{o}_k\}$  for the point  $\mathbf{p}_k$ ;
- Obtain the codes  $\{\sigma_{k'}, \mathbf{c}_{k'}, \mathbf{o}_{k'}\}$  for the inverse point  $\mathbf{p}_{k'}$ ;
- *Tackle visual occlusions:*  
 if  $\mathbf{o}_k = \mathbf{o}_t$  and  $\mathbf{o}_k \neq \hat{\mathbf{o}}$  do:  $\mathbf{o}_k \leftarrow \hat{\mathbf{o}}$   
*Note: the target object is behind the surface but will be manipulated;*
- Obtain new implicit codes  $\{\bar{\sigma}_k, \bar{\mathbf{c}}_k, \bar{\mathbf{o}}_k\}$  for  $\mathbf{p}_k$  after manipulation:  
 if  $\mathbf{o}_k \neq \mathbf{o}_t$  and  $o_k^{H+1} \neq 1$  and  $\mathbf{o}_{k'} = \mathbf{o}_t$  do: collision detected, EXIT.  
 if  $\mathbf{o}_k \neq \mathbf{o}_t$  and  $\mathbf{o}_{k'} = \mathbf{o}_t$  do:  $\{\bar{\sigma}_k, \bar{\mathbf{c}}_k, \bar{\mathbf{o}}_k\} \leftarrow \{\sigma_{k'}, \mathbf{c}_{k'}, \mathbf{o}_{k'}\}$  ;  
 if  $\mathbf{o}_k = \mathbf{o}_t$  and  $\mathbf{o}_{k'} = \mathbf{o}_t$  do:  $\{\bar{\sigma}_k, \bar{\mathbf{c}}_k, \bar{\mathbf{o}}_k\} \leftarrow \{\sigma_{k'}, \mathbf{c}_{k'}, \mathbf{o}_{k'}\}$  ;  
 if  $\mathbf{o}_k = \mathbf{o}_t$  and  $\mathbf{o}_{k'} \neq \mathbf{o}_t$  do:  $\{\bar{\sigma}_k, \bar{\mathbf{c}}_k, \bar{\mathbf{o}}_k\} \leftarrow \{0, \mathbf{0}, \mathbf{0}\}$  ;  
 if  $\mathbf{o}_k \neq \mathbf{o}_t$  and  $\mathbf{o}_{k'} \neq \mathbf{o}_t$  do:  $\{\bar{\sigma}_k, \bar{\mathbf{c}}_k, \bar{\mathbf{o}}_k\} \leftarrow \{\sigma_k, \mathbf{c}_k, \mathbf{o}_k\}$  ;

After the above *for loop*, every point  $\mathbf{p}_k$  will get new implicit codes  $\{\bar{\sigma}_k, \bar{\mathbf{c}}_k, \bar{\mathbf{o}}_k\}$ .

*NOTE: The step below shows how to project edited 3D points to a 2D image.*

According to volume rendering equation, the final pixel color and object code are:

$$\bullet \bar{\mathbf{c}} = \sum_{k=1}^K \bar{T}_k \bar{\alpha}_k \bar{\mathbf{c}}_k, \quad \bar{\mathbf{o}} = \sum_{k=1}^K \bar{T}_k \bar{\alpha}_k \bar{\mathbf{o}}_k$$

where  $\bar{T}_k = \exp(-\sum_{i=1}^{k-1} \bar{\sigma}_i \delta_i)$ ,  $\bar{\alpha}_k = 1 - \exp(-\bar{\sigma}_k \delta_k)$ .

---

- Group 5 (Joint Translation/Rotation/Scaling): One object in each scene is picked up to be simultaneously translated about 0.3 meter, rotated about 90 degrees, scaled down about 0.8× smaller. Then 100 views are generated for testing at the same testing viewpoints in Group 1.

Overall, we create 8 indoor scenes, firstly render the static scenes, and then manipulate each scene followed by second round rendering. We will release this dataset and keep updating it for future research in the community.

**Replica:** Replica [34] is a reconstruction-based 3D dataset of high fidelity scenes. We request the authors of Semantic-NeRF [48] to generate (180 training + 180 testing) color images and 2D object masks with camera poses at  $640 \times 480$  pixels for each of 7 scenes. Each scene has 59 ~ 93 objects with very diverse sizes. Details of camera settings and trajectories can be found in [48].

**ScanNet:** ScanNet [8] is a large-scale challenging real-world dataset. We select 8 scenes for evaluation. Each scene has about 3000 raw images with 2D

object masks and camera poses, among which we evenly select 300 images/masks for training and 100 for testing. There are around 10 objects in each scene.

## 4.2 Baseline and Metrics

The only recent work relevant to us is [42], but its design is vastly different:

- It requires a point cloud as input for voxelization in training, but we do not.
- It needs GT bounding boxes of target objects to manually prune point samples during editing. Therefore, it needs manual annotations on novel views to finish editing. However, we do not need any annotations in editing.
- It only learns to binarily segment the foreground object and background, by pre-defining an Object Activation Code Library during training and editing. However, the object code of our method is completely learned from scratch.

This means that the work [42] is not comparable due to the fundamental differences in design and evaluation. Note that, the recent Semantic-NeRF [48] is also not comparable because it only learns 3D semantic categories, not segments individual objects. Considering that our pipeline is trained and tested with 2D images and masks, we turn to use the classic Mask-RCNN [14] as a solid baseline. We hope that our DM-NeRF could serve as the first baseline for 3D scene decomposition and manipulation in the future.

**Mask-RCNN:** Since we train our DM-NeRF network in scene-specific fashion, we also fine-tune a COCO-pretrained R50-FPN Mask R-CNN model released by Detectron2 Library on every single scene as well. In particular, we carefully fine-tune the model using up to 480 epochs with learning rate  $5e^{-4}$  and then pick up the best model on the testing split of every scene for comparison.

**Metrics:** We use the standard PSNR/SSIM/LPIPS scores to evaluate color image synthesis [21], and use AP of all 2D testing images to evaluate 3D scene decomposition. Note that object classification is irrelevant in this paper.

## 4.3 3D Scene Decomposition

We evaluate the performance of scene decomposition on three datasets. Note that, for DM-SR dataset, we evaluate our method and the baseline on images of Group 1 only, while the images of Groups 2/3/4/5 are used for object manipulation. For every single scene in the three datasets, we train a separate model for our method, and fine-tune a separate model for Mask-RCNN for fairness.

Tables 1/2/3 show the quantitative results on three datasets. It can be seen that our method, not surprisingly, achieves excellent results for novel view rendering thanks to the original NeRF backbone. Notably, our method obtains nearly perfect object segmentation results across multiple viewing points of complex 3D scenes in all three datasets, clearly outperforming the baseline. We also provide additional quantitative results of AP scores with IoU threshold at 0.9 in appendix to show the clear gaps between our method and Mask-RCNN. Figure 6 shows the qualitative results and we can see that our results have much sharper object boundaries thanks to the explicit 3D geometry applied in our object field.

|                 | Novel View Synthesis |                 |                    | Decomposition                |              |                               |              |
|-----------------|----------------------|-----------------|--------------------|------------------------------|--------------|-------------------------------|--------------|
|                 | PSNR $\uparrow$      | SSIM $\uparrow$ | LPIPS $\downarrow$ | MR[14]                       | <b>Ours</b>  | MR[14]                        | <b>Ours</b>  |
| Synthetic Rooms |                      |                 |                    | AP <sup>0.5</sup> $\uparrow$ |              | AP <sup>0.75</sup> $\uparrow$ |              |
| Bathroom        | 44.05                | 0.994           | 0.009              | 97.90                        | 100.0        | 93.81                         | 100.0        |
| Bedroom         | 48.07                | 0.996           | 0.009              | 98.91                        | 100.0        | 97.92                         | 100.0        |
| Dinning         | 42.34                | 0.984           | 0.028              | 98.85                        | 100.0        | 98.85                         | 99.66        |
| Kitchen         | 46.06                | 0.994           | 0.014              | 92.06                        | 100.0        | 92.04                         | 100.0        |
| Reception       | 42.59                | 0.993           | 0.008              | 98.81                        | 100.0        | 98.81                         | 100.0        |
| Rest            | 42.80                | 0.994           | 0.007              | 98.89                        | 100.0        | 98.89                         | 99.89        |
| Study           | 41.08                | 0.987           | 0.026              | 98.93                        | 99.69        | 96.86                         | 98.86        |
| Office          | 46.38                | 0.996           | 0.006              | 96.87                        | 100.0        | 97.83                         | 100.0        |
| Average         | 44.17                | 0.992           | 0.013              | 97.65                        | <b>99.96</b> | 96.87                         | <b>99.80</b> |

**Table 1.** Quantitative results of our method on 8 scenes of DM-SR dataset.

|                     | Novel View Synthesis |                 |                    | Decomposition                |              |                               |              |
|---------------------|----------------------|-----------------|--------------------|------------------------------|--------------|-------------------------------|--------------|
|                     | PSNR $\uparrow$      | SSIM $\uparrow$ | LPIPS $\downarrow$ | MR[14]                       | <b>Ours</b>  | MR[14]                        | <b>Ours</b>  |
| Reconstructed Rooms |                      |                 |                    | AP <sup>0.5</sup> $\uparrow$ |              | AP <sup>0.75</sup> $\uparrow$ |              |
| Office_0            | 40.66                | 0.972           | 0.070              | 90.88                        | 94.40        | 74.05                         | 82.71        |
| Office_2            | 36.98                | 0.964           | 0.115              | 90.07                        | 93.75        | 73.41                         | 81.12        |
| Office_3            | 35.34                | 0.955           | 0.078              | 88.97                        | 89.43        | 72.91                         | 76.30        |
| Office_4            | 32.95                | 0.921           | 0.172              | 82.09                        | 83.60        | 74.76                         | 70.33        |
| Room_0              | 34.97                | 0.940           | 0.127              | 86.84                        | 93.45        | 78.67                         | 79.83        |
| Room_1              | 34.72                | 0.931           | 0.134              | 87.04                        | 96.97        | 78.38                         | 92.11        |
| Room_2              | 37.32                | 0.963           | 0.115              | 84.75                        | 93.85        | 77.58                         | 84.78        |
| Average             | 36.13                | 0.949           | 0.116              | 87.23                        | <b>92.21</b> | 75.68                         | <b>81.03</b> |

**Table 2.** Quantitative results of our method on 7 scenes of Replica dataset.

|                  | Novel View Synthesis |                 |                    | Decomposition                |              |                               |              |
|------------------|----------------------|-----------------|--------------------|------------------------------|--------------|-------------------------------|--------------|
|                  | PSNR $\uparrow$      | SSIM $\uparrow$ | LPIPS $\downarrow$ | MR[14]                       | <b>Ours</b>  | MR[14]                        | <b>Ours</b>  |
| Real-world Rooms |                      |                 |                    | AP <sup>0.5</sup> $\uparrow$ |              | AP <sup>0.75</sup> $\uparrow$ |              |
| 0010.00          | 26.82                | 0.809           | 0.381              | 92.80                        | 97.24        | 83.90                         | 94.82        |
| 0012.00          | 29.28                | 0.753           | 0.389              | 93.49                        | 99.80        | 86.90                         | 98.86        |
| 0024.00          | 23.68                | 0.705           | 0.452              | 87.18                        | 97.20        | 69.87                         | 93.25        |
| 0033.00          | 27.76                | 0.856           | 0.342              | 93.74                        | 98.83        | 88.70                         | 97.02        |
| 0038.00          | 29.36                | 0.716           | 0.415              | 97.01                        | 99.43        | 96.01                         | 99.17        |
| 0088.00          | 29.37                | 0.825           | 0.386              | 90.04                        | 91.50        | 69.06                         | 83.59        |
| 0113.00          | 31.19                | 0.878           | 0.320              | 98.59                        | 99.67        | 98.59                         | 98.67        |
| 0192.00          | 28.19                | 0.732           | 0.376              | 97.94                        | 100.0        | 96.95                         | 99.40        |
| Average          | 28.21                | 0.784           | 0.383              | 93.85                        | <b>97.96</b> | 86.25                         | <b>95.60</b> |

**Table 3.** Quantitative results of our method on 8 scenes of ScanNet dataset.

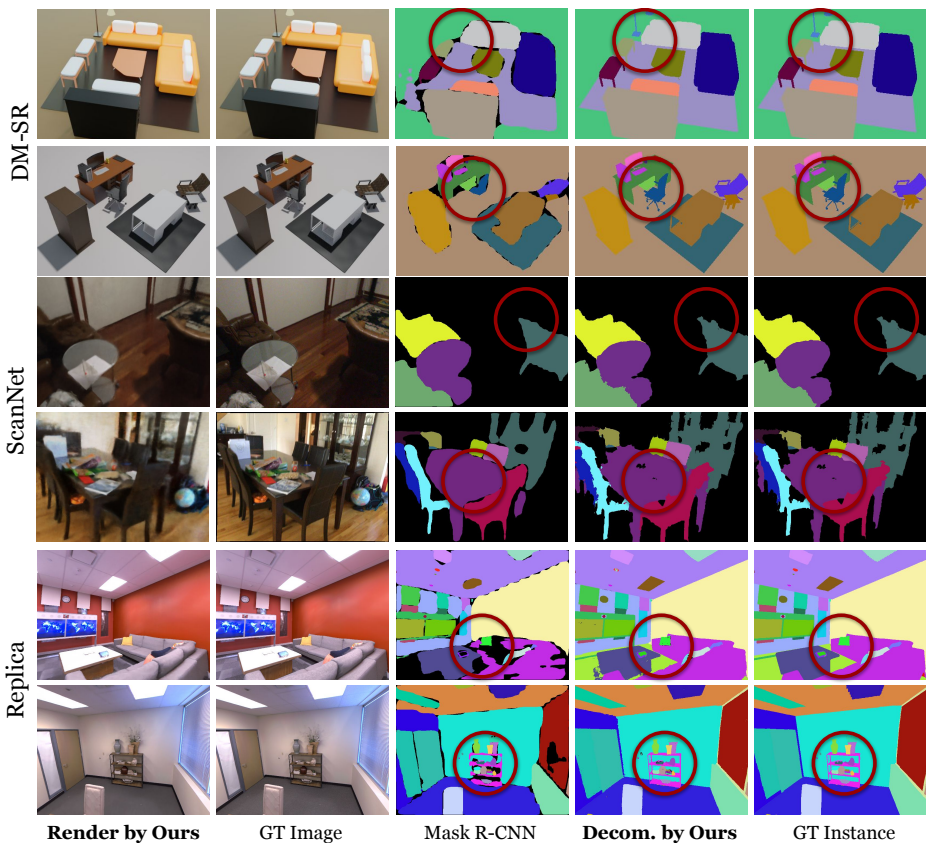


**Fig. 6.** Qualitative results of our method and baselines on three datasets: DM-SR, Replica and ScanNet. The dark red circles highlight the differences.

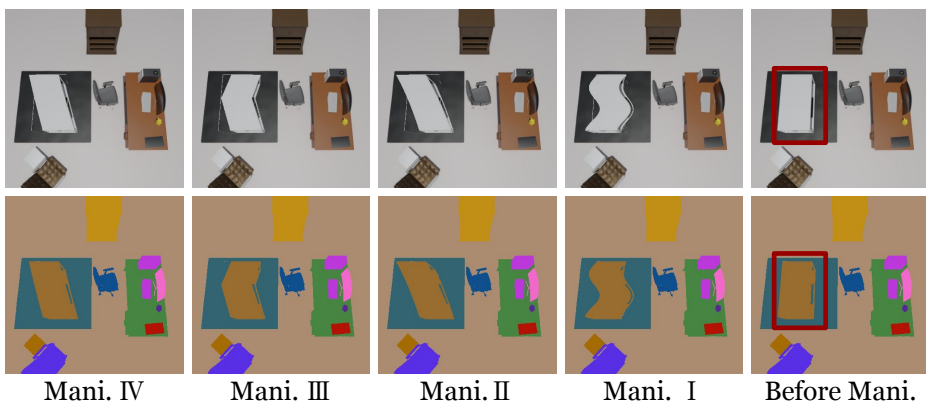


**Fig. 7.** Qualitative results of our method for object deformation manipulation on DM-SR dataset. The dark red boxes highlight the differences.

## 4.4 3D Object Manipulation

In this section, we directly use our model trained on the images of Group 1 to test on the remaining images of Groups 2/3/4/5 in DM-SR dataset. In particular, with the trained model, we feed the known manipulation information of Groups 2/3/4/5 into Algorithm 1, generating images and 2D object masks. These (edited) images and masks are compared with the ground truth 2D views.

Table 4 shows the quantitative results. More strict AP scores with IoU=0.9 are used to better show the difference of object segmentation. It can be seen that the quality of novel view rendering decreases after manipulation compared with non-manipulation in Table 1, primarily because the lighting factors are not decomposed and the illumination of edited objects shows discrepancies. However, the object decomposition is still nearly perfect, as also shown in Figure 8. Moreover, Figure 7 shows additional qualitative results of deformation manipulation.

## 4.5 Ablation Study

To evaluate the effectiveness of our key designs of object field and manipulator, we conduct two ablation studies. 1) We only remove the loss functions ( $\ell_{3d\_empty} + \ell_{3d\_obj}$ ) which are jointly designed to learn correct codes for empty 3D points, denoted as w/o  $\ell_{3d}$ . 2) During manipulation, we remove the step ‘‘Tackle visual occlusions’’ in Algorithm 1, denoted as w/o VO. As shown in Table 4, both our loss functions for empty space regularization and visual occlusion handling step are crucial for accurate 3D scene decomposition and manipulation. More ablation results are in appendix.

|                 | Translation     |                 |                    |                     | Rotation        |                 |                    |                     |
|-----------------|-----------------|-----------------|--------------------|---------------------|-----------------|-----------------|--------------------|---------------------|
|                 | PSNR $\uparrow$ | SSIM $\uparrow$ | LPIPS $\downarrow$ | AP $^{0.9}\uparrow$ | PSNR $\uparrow$ | SSIM $\uparrow$ | LPIPS $\downarrow$ | AP $^{0.9}\uparrow$ |
| w/o $\ell_{3d}$ | 32.84           | 0.967           | 0.048              | 87.26               | 30.38           | 0.945           | 0.090              | 82.46               |
| w/o VO          | 33.54           | 0.970           | 0.045              | 86.93               | 30.57           | 0.953           | 0.076              | 82.43               |
| Ours (Full)     | <b>33.94</b>    | <b>0.975</b>    | <b>0.033</b>       | <b>89.33</b>        | <b>31.94</b>    | <b>0.969</b>    | <b>0.038</b>       | <b>85.68</b>        |
|                 | Scale           |                 |                    |                     | Joint           |                 |                    |                     |
|                 | PSNR $\uparrow$ | SSIM $\uparrow$ | LPIPS $\downarrow$ | AP $^{0.9}\uparrow$ | PSNR $\uparrow$ | SSIM $\uparrow$ | LPIPS $\downarrow$ | AP $^{0.9}\uparrow$ |
| w/o $\ell_{3d}$ | 31.84           | 0.959           | 0.062              | 83.31               | 29.95           | 0.947           | 0.088              | 77.36               |
| w/o VO          | 32.43           | 0.964           | 0.054              | 76.33               | 29.85           | 0.951           | 0.075              | 74.71               |
| Ours (Full)     | <b>33.40</b>    | <b>0.971</b>    | <b>0.037</b>       | <b>86.05</b>        | <b>30.65</b>    | <b>0.965</b>    | <b>0.045</b>       | <b>81.70</b>        |

**Table 4.** Quantitative results of our object manipulation results on DM-SR dataset.

## 5 Discussion and Conclusion

We have shown that it is feasible to simultaneously reconstruct, decompose, manipulate and render complex 3D scenes in a single pipeline only from 2D views. By adding an object field component into the MLP based implicit representation, we can successfully decompose all individual objects in 3D space. The decomposed object shapes can be further freely edited using our visual occlusion aware manipulator. The limitation of our work is the lack of decomposing lighting factors, which is left for our future work.

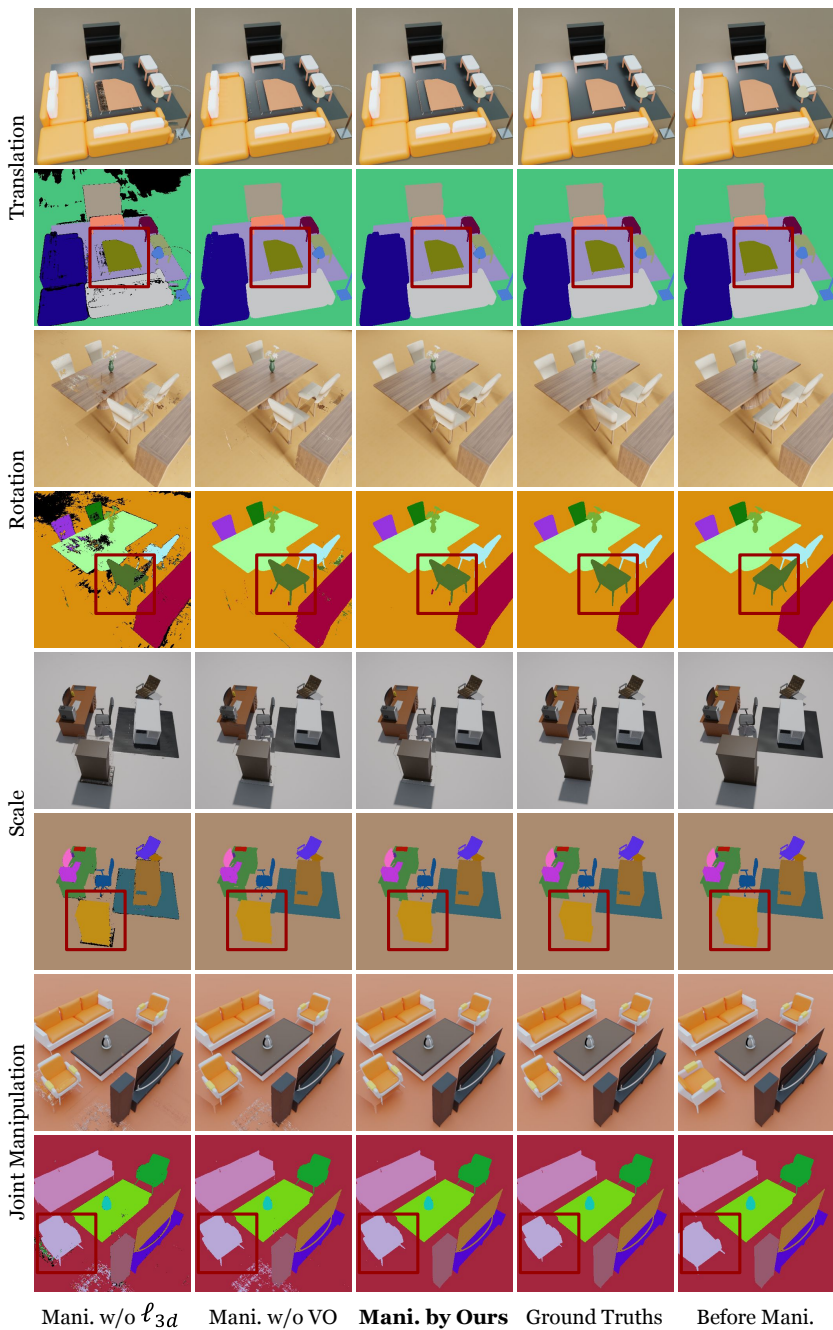


**Fig. 8.** Qualitative results of our method for object manipulation on DM-SR dataset. The dark red boxes highlight the differences.

## References

1. Alaluf, Y., Mokady, R., Bermano, A.H.: HyperStyle: StyleGAN Inversion with HyperNetworks for Real Image Editing. CVPR (2022)
2. Alliez, P., Meyer, M., Desbrun, M.: Interactive geometry remeshing. ACM TOG (2002)
3. Boss, M., Jampani, V., Braun, R., Liu, C., Barron, J.T., Hendrik: Neural-PIL: Neural Pre-Integrated Lighting for Reflectance Decomposition. NeurIPS (2021)
4. Cadena, C., Carlone, L., Carrillo, H., Latif, Y., Scaramuzza, D., Neira, J., Reid, I.D., Leonard, J.J.: Past, Present, and Future of Simultaneous Localization and Mapping: Towards the Robust-Perception Age. IEEE Transactions on Robotics (2016)
5. Chen, W., Litalien, J., Gao, J., Wang, Z., Tsang, C.F., Khamis, S., Litany, O., Fidler, S.: DIB-R++: Learning to Predict Lighting and Material with a Hybrid Differentiable Renderer. NeurIPS (2021)
6. Chibane, J., Mir, A., Pons-Moll, G.: Neural Unsigned Distance Fields for Implicit Function Learning. NeurIPS (2020)
7. Choy, C.B., Xu, D., Gwak, J., Chen, K., Savarese, S.: 3D-R2N2: A Unified Approach for Single and Multi-view 3D Object Reconstruction. ECCV (2016)
8. Dai, A., Chang, A.X., Savva, M., Halber, M., Funkhouser, T., Nießner, M.: ScanNet: Richly-annotated 3D Reconstructions of Indoor Scenes. CVPR (2017)
9. Dharmo, H., Manhardt, F., Navab, N., Tombari, F.: Graph-to-3D: End-to-End Generation and Manipulation of 3D Scenes Using Scene Graphs. ICCV (2021)
10. Fan, H., Su, H., Guibas, L.: A Point Set Generation Network for 3D Object Reconstruction from a Single Image. CVPR (2017)
11. Gkioxari, G., Malik, J., Johnson, J.: Mesh R-CNN. ICCV (2019)
12. Groueix, T., Fisher, M., Kim, V.G., Russell, B.C., Aubry, M.: A Papier-Mache Approach to Learning 3D Surface Generation. CVPR (2018)
13. Guandao Yang, Belongie, S., Hariharan, B., Koltun, V.: Geometry Processing with Neural Fields. NeurIPS (2021)
14. He, K., Gkioxari, G., Dollar, P., Girshick, R.: Mask R-CNN. IEEE International Conference on Computer Vision pp. 2961–2969 (2017)
15. Jang, W., Agapito, L.: CodeNeRF: Disentangled Neural Radiance Fields for Object Categories. ICCV (2021)
16. Kato, H., Ushiku, Y., Harada, T.: Neural 3D Mesh Renderer. CVPR (2018)
17. Kuhn, H.W.: The Hungarian Method for the assignment problem. Naval Research Logistics Quarterly **2**(1-2), 83–97 (1955)
18. Lin, C.H., Kong, C., Lucey, S.: Learning Efficient Point Cloud Generation for Dense 3D Object Reconstruction. AAAI (2018)
19. Liu, S., Zhang, X., Zhang, Z., Zhang, R., Zhu, J.Y., Russell, B.: Editing Conditional Radiance Fields. ICCV (2021)
20. Mescheder, L., Oechsle, M., Niemeyer, M., Nowozin, S., Geiger, A.: Occupancy Networks: Learning 3D Reconstruction in Function Space. CVPR (2019)
21. Mildenhall, B., Srinivasan, P.P., Tancik, M., Barron, J.T., Ramamoorthi, R., Ng, R.: NeRF: Representing Scenes as Neural Radiance Fields for View Synthesis. ECCV (2020)
22. Mousavian, A., Anguelov, D., Flynn, J., Kosecka, J.: 3D Bounding Box Estimation Using Deep Learning and Geometry. CVPR (2017)
23. Munkberg, J., Hasselgren, J., Shen, T., Gao, J., Chen, W., Evans, A., Müller, T., Fidler, S.: Extracting Triangular 3D Models, Materials, and Lighting From Images. arXiv:2111.12503 (2021)

24. Niemeyer, M., Geiger, A.: GIRAFFE: Representing Scenes as Compositional Generative Neural Feature Fields. CVPR pp. 11453–11464 (2021)
25. Niemeyer, M., Mescheder, L., Oechsle, M., Geiger, A.: Differentiable Volumetric Rendering: Learning Implicit 3D Representations without 3D Supervision. CVPR (2020)
26. Ost, J., Mannan, F., Thuerey, N., Knodt, J., Heide, F.: Neural Scene Graphs for Dynamic Scenes. CVPR (2021)
27. Ozyesil, O., Voroninski, V., Basri, R., Singer, A.: A Survey of Structure from Motion. *Acta Numerica* **26**, 305–364 (2017)
28. Park, J.J., Florence, P., Straub, J., Newcombe, R., Lovegrove, S.: DeepSDF: Learning Continuous Signed Distance Functions for Shape Representation. CVPR (2019)
29. Roberts, M., Paczan, N.: Hypersim: A Photorealistic Synthetic Dataset for Holistic Indoor Scene Understanding. ICCV (2021)
30. Savva, M., Kadian, A., Maksymets, O., Zhao, Y., Wijmans, E., Jain, B., Straub, J., Liu, J., Koltun, V., Malik, J., Parikh, D., Batra, D.: Habitat: A Platform for Embodied AI Research. ICCV (2019)
31. Sengupta, S., Gu, J., Kim, K., Liu, G., Jacobs, D.W., Kautz, J.: Neural Inverse Rendering of an Indoor Scene from a Single Image. ICCV (2019)
32. Song, S., Yu, F., Zeng, A., Chang, A.X., Savva, M., Funkhouser, T.: Semantic Scene Completion from a Single Depth Image. CVPR (2017)
33. Stelzner, K., Kersting, K., Kosiorek, A.R.: Decomposing 3D Scenes into Objects via Unsupervised Volume Segmentation. arXiv:2104.01148 (2021)
34. Straub, J., Whelan, T., Ma, L., Chen, Y., Wijmans, E., Green, S., Engel, J.J., Mur-artal, R., Ren, C., Verma, S., Clarkson, A., Yan, M., Budge, B., Yan, Y., Pan, X., Yon, J., Zou, Y., Leon, K., Carter, N., Briales, J., Gillingham, T., Mueggler, E., Pesqueira, L., Savva, M., Batra, D., Strasdat, H.M.: The Replica Dataset : A Digital Replica of Indoor Spaces. arXiv:1906.05797 (2019)
35. Tatarchenko, M., Dosovitskiy, A., Brox, T.: Octree Generating Networks: Efficient Convolutional Architectures for High-resolution 3D Outputs. ICCV (2017)
36. Tewari, A., Elgharib, M., Bharaj, G., Bernard, F., Seidel, H.P., Perez, P., Zollhofer, M., Theobalt, C.: StyleRig: Rigging StyleGAN for 3D Control over Portrait Images. CVPR (2020)
37. Trevithick, A., Yang, B.: GRF: Learning a General Radiance Field for 3D Representation and Rendering. ICCV (2021)
38. Tulsiani, S., Gupta, S., Fouhey, D., Efros, A.A., Malik, J.: Factoring Shape, Pose, and Layout from the 2D Image of a 3D Scene. CVPR (2018)
39. Wang, B., Yu, Z., Yang, B., Qin, J., Breckon, T., Shao, L., Trigoni, N., Markham, A.: RangeUDF: Semantic Surface Reconstruction from 3D Point Clouds. arXiv:2204.09138 (2022)
40. Wang, P., Liu, L., Liu, Y., Theobalt, C., Komura, T., Wang, W.: NeuS: Learning Neural Implicit Surfaces by Volume Rendering for Multi-view Reconstruction. NeurIPS (2021)
41. Xie, H., Yao, H., Sun, X., Zhou, S., Zhang, S., Tong, X.: Pix2Vox: Context-aware 3D Reconstruction from Single and Multi-view Images. ICCV (2019)
42. Yang, B., Zhang, Y., Xu, Y., Li, Y., Zhou, H., Bao, H., Zhang, G., Cui, Z.: Learning Object-Compositional Neural Radiance Field for Editable Scene Rendering. ICCV (2021)
43. Yang, B., Rosa, S., Markham, A., Trigoni, N., Wen, H.: Dense 3D Object Reconstruction from a Single Depth View. *IEEE Transactions on Pattern Analysis and Machine Intelligence* (2019)



44. Yang, B., Wang, J., Clark, R., Hu, Q., Wang, S., Markham, A., Trigoni, N.: Learning Object Bounding Boxes for 3D Instance Segmentation on Point Clouds. *NeurIPS* (2019)
45. Zhang, C., Cui, Z., Zhang, Y., Zeng, B., Pollefeys, M., Liu, S.: Holistic 3D Scene Understanding from a Single Image with Implicit Representation. *CVPR* (2021)
46. Zhang, J., Liu, X., Ye, X., Zhao, F., Zhang, Y., Wu, M., Zhang, Y., Xu, L., Yu, J.: Editable free-viewpoint video using a layered neural representation. *ACM Transactions on Graphics* **40**(4) (2021)
47. Zhang, X., Srinivasan, P.P., Deng, B., Debevec, P., Freeman, W.T., Barron, J.T.: NeRFactor: Neural Factorization of Shape and Reflectance Under an Unknown Illumination. *SIGGRAPH Asia* (2021)
48. Zhi, S., Laidlow, T., Leutenegger, S., Davison, A.J.: In-Place Scene Labelling and Understanding with Implicit Scene Representation. *ICCV* (2021)
49. Zhou, Y., Tuzel, O.: VoxelNet: End-to-End Learning for Point Cloud Based 3D Object Detection. *CVPR* (2018)
50. Zou, C., Yumer, E., Yang, J., Ceylan, D., Hoiem, D.: 3D-PRNN: Generating Shape Primitives with Recurrent Neural Networks. *ICCV* (2017)

## A Additional Implementation Details

**Network Architecture** The detailed architecture of our simple pipeline is shown in Figure 9.

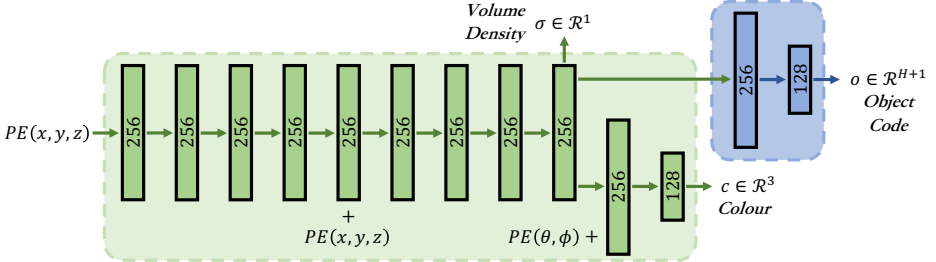


**Fig. 9.** DM-NeRF network architecture. The positional encoding  $PE(\cdot)$  of the location  $(x, y, z)$  and viewing direction  $(\theta, \phi)$  are taken as the inputs of our network. The volume density  $\sigma$  and object code  $\mathbf{o}$  are the functions of the location while the colour additionally depends on the viewing direction.

**2D Object Matching and Supervision** As illustrated in Figure 3, assuming we generate  $L$  images of 2D object predictions  $\{I_1 \dots I_l \dots I_L\}$ ,  $I_l \in \mathbf{R}^{U \times V \times (H+1)}$  and have the paired  $L$  images of 2D ground truth object labels  $\{\bar{I}_1 \dots \bar{I}_l \dots \bar{I}_L\}$ ,  $\bar{I}_l \in \mathbf{R}^{U \times V \times T}$ , in which  $H$  is the predefined number of objects and  $T$  represents the number of ground truth objects.

For each pair, we firstly take the first  $H$  solid object predictions of  $I$  and reshape it to  $M \in \mathbf{R}^{N \times H}$ , where  $N = U \times V$ . Likewise,  $\bar{I}$  is reshaped to  $\bar{M} \in \mathbf{R}^{N \times T}$ . Then,  $M$  and  $\bar{M}$  are fed into Hungarian algorithm [17] to associate every ground truth 2D object mask with a unique predicted 2D object mask according to Soft Intersection-over-Union (sIoU) and Cross-Entropy Score (CES) [44].

Formally, the Soft Intersection-over-Union (sIoU) cost between the  $h^{th}$  predicted box and the  $t^{th}$  ground truth box in the  $l^{th}$  pair is defined as follows:

$$\mathcal{C}_{h,t}^{sIoU} = \frac{\sum_{n=1}^N (M_h^n * \bar{M}_t^n)}{\sum_{n=1}^N M_h^n + \sum_{n=1}^N \bar{M}_t^n - \sum_{n=1}^N (M_h^n * \bar{M}_t^n)} \quad (9)$$

where  $M_h^n$  and  $\bar{M}_t^n$  are the  $n^{th}$  values of  $M_i$  and  $\bar{M}_t$ . In addition, we also consider the cross-entropy score between  $M_h$  and  $\bar{M}_t$  which is formally defined as:

$$\mathcal{C}_{h,t}^{CES} = -\frac{1}{N} \sum_{n=1}^N [\bar{M}_t^n \log M_h^n + (1 - \bar{M}_t^n) \log(1 - M_h^n)] \quad (10)$$

After association, we reorder the predicted object masks to align with the  $T$  ground truth masks, and then we directly minimize the cost values of all ground truth objects in every pair of images.

$$sIoU_l = \frac{1}{T} \sum_{t=1}^T (C_{t,t}^{sIoU}) \quad CES_l = \frac{1}{T} \sum_{t=1}^T (C_{t,t}^{CES}) \quad (11)$$

**Training Details** For all experiments, we set the batch size as 3072 rays just to fully use the memory. For each ray, we sample 64 points and 128 additional points in the coarse and fine volume, respectively. The Adam optimizer with default hyper-parameters ( $\beta_1 = 0.9$ ,  $\beta_2 = 0.999$ , and  $\epsilon = 10^{-7}$ ) is exploited. The learning rate is set to  $5 \times 10^{-4}$  and decays exponentially to  $5 \times 10^{-5}$  over the course of optimization. The optimization for a single scene typically take around 200–300k iterations to converge on a single NVIDIA RTX3090 GPU (about 17–25 hours).

**Evaluation Details** We use the MASK-RCNN code open-sourced by the Matterport at [https://github.com/matterport/Mask\\_RCNN](https://github.com/matterport/Mask_RCNN) and follow their procedure to calculate the AP values. Note that, we regard IoU values as scores during the ranking procedure.

## B Additional Dataset Details

To quantitatively evaluate geometry manipulation, we create a synthetic dataset with 8 types of different and complex indoor rooms (shown in Figure 11), called DM-SR, containing path-traced images that exhibit complicated geometry. The room types and designs follow Hypersim dataset [29].

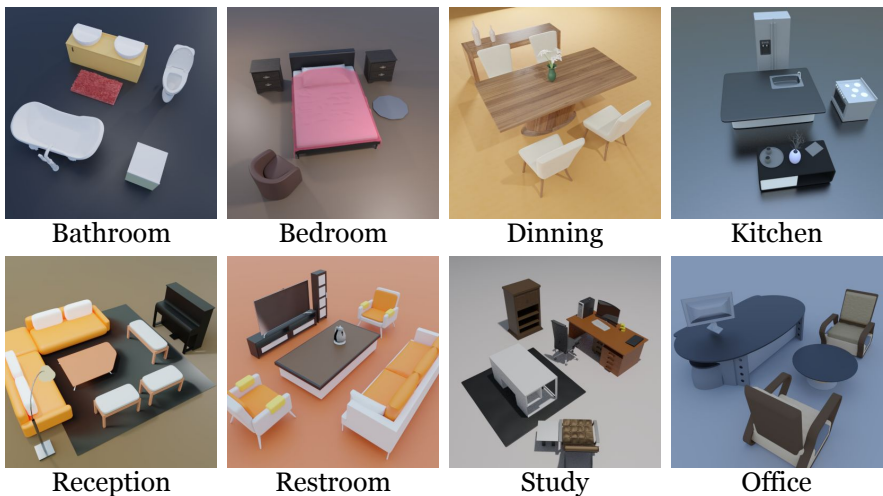


Fig. 10. Eight different indoor scenes of our DM-SR dataset.

In our new dataset, 13 common classes of objects (chair, desk, television, fridge, bathtub, etc.) are introduced. The raw object meshes are downloaded from <https://free3d.com/>. We apply different scale/pose transformations on objects and then compose eight common indoor rooms, including bathroom, dining room, restroom, etc.. We follow the default world coordinate system in Blender: the positive x, y and z axes pointing right, forward and up, respectively.

To increase realism, we set various types of textures and environment lights for different objects and scenes. Four commonly used types of lights (point, sun, spot, area) are included and the strength is limited within 1000W. During rendering, a camera with 50 degrees field of view is added to generate RGB, depth, semantic and instance images at the resolution of 400×400 pixels. For each scene, the training RGB images are rendered from viewpoints randomly sampled on the upper hemisphere. The viewpoints of testing images are sampled following a smooth spiral trajectory. In addition, instance images are generated by the ray cast function built in Blender.

## C Additional Quantitative Results

*Ablations of MaskRCNN* We provide additional quantitative results of AP scores with IoU thresholds at 0.5 and 0.75 in Table 5 to compare four groups of experiments for MaskRCNN on the selected eight scenes of ScanNet.

|         | AP <sup>0.50</sup> ↑ |              |       |              | AP <sup>0.75</sup> ↑ |       |              |              |
|---------|----------------------|--------------|-------|--------------|----------------------|-------|--------------|--------------|
|         | G_1                  | G_2          | G_3   | G_4          | G_1                  | G_2   | G_3          | G_4          |
| 0010_00 | 88.34                | 91.77        | 90.58 | 92.80        | 76.30                | 74.51 | 82.61        | 83.90        |
| 0012_00 | 89.89                | 92.68        | 93.63 | 93.49        | 85.76                | 82.77 | 86.35        | 86.90        |
| 0024_00 | 83.45                | 87.15        | 84.26 | 87.18        | 57.46                | 49.38 | 67.08        | 69.87        |
| 0033_00 | 92.81                | 93.94        | 93.69 | 93.74        | 88.42                | 87.59 | 88.93        | 88.70        |
| 0038_00 | 96.98                | 96.99        | 96.94 | 97.01        | 95.92                | 94.88 | 95.87        | 96.01        |
| 0088_00 | 85.01                | 88.07        | 85.95 | 90.04        | 63.29                | 94.88 | 73.34        | 69.06        |
| 0113_00 | 97.97                | 98.12        | 97.60 | 98.59        | 97.60                | 98.59 | 98.17        | 98.59        |
| 0192_00 | 97.78                | 97.79        | 97.78 | 97.94        | 96.76                | 95.79 | 95.26        | 96.95        |
| Average | 91.53                | <u>93.31</u> | 92.55 | <b>93.85</b> | 82.69                | 84.80 | <u>85.95</u> | <b>86.25</b> |

**Table 5.** Average scores of MaskRCNN on 8 scenes of ScanNet.

- **Group 1 (G\_1):** Train a single MaskRCNN model on the 8 scenes together from scratch, and then evaluate.
- **Group 2 (G\_2):** Load a single pretrained MaskRCNN model, and then finetune and evaluate it on the 8 scenes together.
- **Group 3 (G\_3):** Train 8 MaskRCNN models on the 8 scenes separately from scratch, and then evaluate respectively.
- **Group 4 (G\_4):** Load 8 copies of the pretrained model, and then finetune and evaluate on 8 scenes separately.

Table 5 shows that Group 4 achieves the highest scores, which also has the fairest experimental settings we can set up for comparison.

**Ablations of the Object Field** Since the backbone of our pipeline is completely the same as the original NeRF, and our proposed object field component is supervised by  $\ell_{2d\_obj}$  from 2D signals and by  $(\ell_{3d\_empty} + \ell_{3d\_obj})$  from 3d signals. Note that, the losses  $(\ell_{3d\_empty} + \ell_{3d\_obj})$  only involve a single hyperparameter  $\Delta d$  as shown in Equations 5/6/7. To comprehensively evaluate the effectiveness of these components, we conduct additional experiments with the following ablated versions of our object field along with our main experiments.

- Without  $(\ell_{3d\_empty} + \ell_{3d\_obj})$ : Basically, these two losses are jointly designed to learn correct codes for empty 3d points. In this case, we only optimize the object field component by  $\ell_{2d\_obj}$  from 2D signals.
- With  $(\ell_{3d\_empty} + \ell_{3d\_obj})$ : We additionally learn correct codes for empty 3d points using such losses but with different  $\Delta d$  (0.025/0.05/0.10 meters).

From Tables 6/7/8, we find that  $\Delta d = 0.05$  achieves better scene decomposition quality. It is also clear that the pipeline trained without  $(\ell_{3d\_empty} + \ell_{3d\_obj})$  has worse AP scores than the pipeline trained with  $(\ell_{3d\_empty} + \ell_{3d\_obj})$ . In fact, different choices of  $\Delta d$  produce very close results, showing that our proposed supervision for empty 3d points is rather robust.

**Ablations of Object Field Training Strategy** To comprehensively evaluate the object field training strategy, we conduct additional experiments with the following ablated versions of training strategy along with our main experiments.

- Without *Detach*: The gradients from object field component can backpropagate to the backbone of NeRF. In this case, the object field part and the rendering part will mutually influence each other.
- With *Detach*: The object field component only depends on the output representation of NeRF and will not affect the rendering part at all.

From Tables 9/10/11, we find the training strategy with *Detach* achieves better scene rendering and decomposition quality in general. It is clear that the rendering quality drops significantly if our object field component is trained without *Detach*. In contrast, when our object field component is trained with *Detach*, better scene rendering quality and comparable decomposition quality are obtained. In this paper, the training strategy with *Detach* is adopted.

| Synthetic<br>Rooms | AP <sup>0.75</sup> ↑ |         |              |        | AP <sup>0.90</sup> ↑ |         |              |        |
|--------------------|----------------------|---------|--------------|--------|----------------------|---------|--------------|--------|
|                    | w/o                  | w/0.025 | w/0.05       | w/0.10 | w/o                  | w/0.025 | w/0.05       | w/0.10 |
| Bathroom           | 100.0                | 100.0   | 100.0        | 100.0  | 98.17                | 97.72   | 98.50        | 98.16  |
| Bedroom            | 100.0                | 100.0   | 100.0        | 100.0  | 100.0                | 100.0   | 100.0        | 100.0  |
| Dinning            | 99.49                | 99.55   | 99.66        | 99.49  | 81.87                | 81.77   | 81.72        | 81.91  |
| Kitchen            | 100.0                | 100.0   | 100.0        | 100.0  | 100.0                | 100.0   | 100.0        | 100.0  |
| Reception          | 100.0                | 100.0   | 100.0        | 100.0  | 100.0                | 100.0   | 100.0        | 100.0  |
| Rest               | 99.88                | 99.89   | 99.89        | 99.89  | 98.77                | 98.97   | 99.03        | 99.03  |
| Study              | 98.77                | 98.81   | 98.86        | 98.71  | 92.19                | 92.31   | 92.15        | 92.12  |
| Office             | 100.0                | 100.0   | 100.0        | 100.0  | 100.0                | 100.0   | 100.0        | 100.0  |
| Average            | 99.77                | 99.78   | <b>99.80</b> | 99.76  | 96.38                | 96.35   | <b>96.43</b> | 96.40  |

**Table 6.** Quantitative results of scene decomposition from our method on DM-SR dataset. AP scores with IoU thresholds at 0.75 and 0.90 are reported.

| Reconstructed<br>Rooms | AP <sup>0.75</sup> ↑ |         |              |        | AP <sup>0.90</sup> ↑ |         |              |        |
|------------------------|----------------------|---------|--------------|--------|----------------------|---------|--------------|--------|
|                        | w/o                  | w/0.025 | w/0.05       | w/0.10 | w/o                  | w/0.025 | w/0.05       | w/0.10 |
| Office_0               | 79.41                | 75.10   | 82.71        | 76.43  | 57.80                | 56.85   | 55.07        | 53.71  |
| Office_2               | 82.77                | 80.83   | 81.12        | 83.70  | 64.68                | 65.02   | 68.34        | 61.18  |
| Office_3               | 67.38                | 78.08   | 76.30        | 75.07  | 48.53                | 54.77   | 55.90        | 53.79  |
| Office_4               | 65.51                | 64.72   | 70.33        | 73.94  | 47.17                | 50.13   | 53.68        | 53.60  |
| Room_0                 | 77.60                | 79.73   | 79.83        | 76.03  | 51.21                | 49.63   | 49.35        | 46.69  |
| Room_1                 | 87.63                | 88.85   | 92.11        | 86.14  | 69.20                | 67.78   | 74.21        | 63.32  |
| Room_2                 | 84.01                | 84.69   | 84.78        | 83.29  | 58.01                | 62.69   | 62.83        | 57.70  |
| Average                | 77.76                | 78.86   | <b>81.03</b> | 79.23  | 56.66                | 58.12   | <b>59.91</b> | 55.71  |

**Table 7.** Quantitative results of scene decomposition from our method on Replica dataset. AP scores with IoU thresholds at 0.75 and 0.90 are reported.

| Real-world<br>Rooms | AP <sup>0.75</sup> ↑ |         |              |        | AP <sup>0.90</sup> ↑ |         |              |        |
|---------------------|----------------------|---------|--------------|--------|----------------------|---------|--------------|--------|
|                     | w/o                  | w/0.025 | w/0.05       | w/0.10 | w/o                  | w/0.025 | w/0.05       | w/0.10 |
| 0010_00             | 95.03                | 94.13   | 94.82        | 94.62  | 86.29                | 86.72   | 90.45        | 86.51  |
| 0012_00             | 99.25                | 99.25   | 98.86        | 99.75  | 94.40                | 95.71   | 95.35        | 94.54  |
| 0024_00             | 78.98                | 84.04   | 93.25        | 78.09  | 56.72                | 58.08   | 72.01        | 53.20  |
| 0033_00             | 94.94                | 92.92   | 97.02        | 95.77  | 89.94                | 87.77   | 93.32        | 88.83  |
| 0038_00             | 96.57                | 97.02   | 99.17        | 96.58  | 93.43                | 92.96   | 97.58        | 93.82  |
| 0088_00             | 83.22                | 82.59   | 83.59        | 78.59  | 61.42                | 58.23   | 59.23        | 61.34  |
| 0113_00             | 92.69                | 92.84   | 98.67        | 98.67  | 85.40                | 85.42   | 96.61        | 96.61  |
| 0192_00             | 97.60                | 97.60   | 99.40        | 99.80  | 96.48                | 96.44   | 98.32        | 98.88  |
| Average             | 92.29                | 92.55   | <b>95.60</b> | 92.74  | 83.01                | 82.66   | <b>87.86</b> | 84.22  |

**Table 8.** Quantitative results of scene decomposition from our method on ScanNet dataset. AP scores with IoU thresholds at 0.75 and 0.90 are reported.

| Detach    | PSNR $\uparrow$ |       | LPIPS $\uparrow$ |       | SSIM $\downarrow$ |       | AP <sup>0.75</sup> $\uparrow$ |       |
|-----------|-----------------|-------|------------------|-------|-------------------|-------|-------------------------------|-------|
|           | w/              | w/o   | w/               | w/o   | w/                | w/o   | w/                            | w/o   |
| Bathroom  | 44.05           | 32.05 | 0.994            | 0.944 | 0.009             | 0.150 | 100.0                         | 100.0 |
| Bedroom   | 48.07           | 32.70 | 0.996            | 0.927 | 0.009             | 0.255 | 100.0                         | 100.0 |
| Dinning   | 42.34           | 33.47 | 0.984            | 0.895 | 0.028             | 0.191 | 99.66                         | 99.29 |
| Kitchen   | 46.06           | 28.49 | 0.994            | 0.904 | 0.014             | 0.221 | 100.0                         | 100.0 |
| Reception | 42.59           | 29.91 | 0.993            | 0.922 | 0.008             | 0.190 | 100.0                         | 99.47 |
| Rest      | 42.80           | 31.33 | 0.994            | 0.930 | 0.007             | 0.145 | 99.89                         | 99.47 |
| Study     | 41.08           | 32.08 | 0.987            | 0.935 | 0.026             | 0.161 | 98.86                         | 98.88 |
| Office    | 46.38           | 32.17 | 0.996            | 0.935 | 0.006             | 0.162 | 100.0                         | 100.0 |
| Average   | <b>44.17</b>    | 31.53 | <b>0.992</b>     | 0.924 | <b>0.013</b>      | 0.185 | <b>99.80</b>                  | 99.71 |

**Table 9.** Quantitative results of our method on DM-SR dataset.

| Detach   | PSNR $\uparrow$ |       | LPIPS $\uparrow$ |       | SSIM $\downarrow$ |       | AP <sup>0.75</sup> $\uparrow$ |              |
|----------|-----------------|-------|------------------|-------|-------------------|-------|-------------------------------|--------------|
|          | w/              | w/o   | w/               | w/o   | w/                | w/o   | w/                            | w/o          |
| Office_0 | 40.66           | 28.20 | 0.972            | 0.781 | 0.070             | 0.422 | 82.71                         | 82.95        |
| Office_2 | 36.98           | 27.98 | 0.964            | 0.837 | 0.115             | 0.361 | 81.12                         | 81.69        |
| Office_3 | 35.34           | 26.68 | 0.955            | 0.817 | 0.078             | 0.366 | 76.30                         | 72.63        |
| Office_4 | 32.95           | 27.19 | 0.921            | 0.804 | 0.172             | 0.363 | 70.33                         | 77.34        |
| Room_0   | 34.97           | 25.18 | 0.940            | 0.682 | 0.127             | 0.403 | 79.83                         | 82.26        |
| Room_1   | 34.72           | 26.54 | 0.931            | 0.717 | 0.134             | 0.425 | 92.11                         | 93.71        |
| Room_2   | 37.32           | 27.43 | 0.963            | 0.786 | 0.115             | 0.392 | 84.78                         | 83.21        |
| Average  | <b>36.13</b>    | 27.03 | <b>0.949</b>     | 0.775 | <b>0.116</b>      | 0.390 | 81.03                         | <b>81.97</b> |

**Table 10.** Quantitative results of our method on Replica dataset.

| Detach  | PSNR $\uparrow$ |       | LPIPS $\uparrow$ |       | SSIM $\downarrow$ |       | AP <sup>0.75</sup> $\uparrow$ |       |
|---------|-----------------|-------|------------------|-------|-------------------|-------|-------------------------------|-------|
|         | w/              | w/o   | w/               | w/o   | w/                | w/o   | w/                            | w/o   |
| 0010_00 | 26.82           | 22.30 | 0.809            | 0.697 | 0.381             | 0.513 | 94.82                         | 97.44 |
| 0012_00 | 29.28           | 22.98 | 0.753            | 0.601 | 0.389             | 0.546 | 98.86                         | 97.67 |
| 0024_00 | 23.68           | 19.41 | 0.705            | 0.552 | 0.452             | 0.573 | 93.25                         | 90.45 |
| 0033_00 | 27.76           | 22.39 | 0.856            | 0.743 | 0.342             | 0.470 | 97.02                         | 97.48 |
| 0038_00 | 29.36           | 24.79 | 0.716            | 0.614 | 0.415             | 0.573 | 99.17                         | 98.42 |
| 0088_00 | 29.37           | 23.87 | 0.825            | 0.692 | 0.386             | 0.513 | 83.59                         | 85.45 |
| 0113_00 | 31.19           | 22.93 | 0.878            | 0.727 | 0.320             | 0.498 | 98.67                         | 99.00 |
| 0192_00 | 28.19           | 21.97 | 0.732            | 0.576 | 0.376             | 0.549 | 99.40                         | 98.75 |
| Average | <b>28.21</b>    | 22.58 | <b>0.784</b>     | 0.650 | <b>0.383</b>      | 0.529 | <b>95.60</b>                  | 95.58 |

**Table 11.** Quantitative results of our method on ScanNet dataset.

| Metric       | AP <sup>0.5</sup> ↑ |       |              |              | AP <sup>0.75</sup> ↑ |       |              |              |
|--------------|---------------------|-------|--------------|--------------|----------------------|-------|--------------|--------------|
|              | MR [14]             |       | <b>Ours</b>  |              | MR [14]              |       | <b>Ours</b>  |              |
| Manipulation | Before              | After | Before       | After        | Before               | After | Before       | After        |
| Bathroom     | 97.90               | 96.36 | 100.0        | 99.38        | 93.81                | 88.89 | 100.0        | 97.57        |
| Bedroom      | 98.91               | 97.14 | 100.0        | 100.0        | 97.92                | 94.84 | 100.0        | 99.38        |
| Dinning      | 98.85               | 98.20 | 100.0        | 99.15        | 98.85                | 96.33 | 99.66        | 97.14        |
| Kitchen      | 92.06               | 93.56 | 100.0        | 100.0        | 92.04                | 91.39 | 100.0        | 98.75        |
| Reception    | 98.81               | 97.03 | 100.0        | 100.0        | 98.81                | 94.63 | 100.0        | 99.40        |
| Rest         | 98.89               | 97.18 | 100.0        | 100.0        | 98.89                | 95.86 | 99.89        | 99.86        |
| Study        | 96.87               | 97.64 | 99.69        | 99.41        | 96.86                | 95.75 | 98.86        | 98.38        |
| Office       | 98.93               | 89.97 | 100.0        | 100.0        | 97.83                | 74.24 | 100.0        | 75.94        |
| Average      | 97.65               | 95.88 | <b>99.96</b> | <u>99.74</u> | 96.87                | 91.49 | <b>99.80</b> | <u>95.80</u> |

**Table 12.** Quantitative results of scene decomposition from our method and Mask-RCNN on DM-SR dataset. AP scores with IoU thresholds at 0.5 and 0.75 are reported.

*Scene Manipulation and Decomposition* To better demonstrate the superiority of our DM-NeRF that simultaneously reconstructs, decomposes, manipulates and renders complex 3D scenes in a single pipeline, we conduct additional experiments with the following comparison of scene decomposition along with our main experiments.

- Decomposition after Manipulation: We manipulate objects within a scene and generate corresponding object masks for decomposition using Mask-RCNN with the weights trained on the same scene before manipulation.
- Simultaneous Manipulation and Decomposition: We appeal to our DM-NeRF to simultaneously manipulate and decompose a scene. The weights we used are also from the same scene but without manipulation.

From Table 12, we can see that, for the same scene, the AP scores reported by Mask-RCNN has an obvious decrease after manipulation. However, our method presents very close AP scores for all scenes before and after manipulation. Fundamentally, this is because Mask-RCNN only considers every 2D image independently for object segmentation, while our DM-NeRF explicitly leverages the consistency between 3D and 2D across multiple views.

## D Additional Qualitative Results

*Scene Rendering and Decomposition* Figures 11/12/13 show additional qualitative results of scene rendering and decomposition.

*Scene Manipulation* Figures 14/15 shows additional qualitative results of scene manipulation with single/multiple objects under various transformations.

More qualitative results can be found in the supplied video.



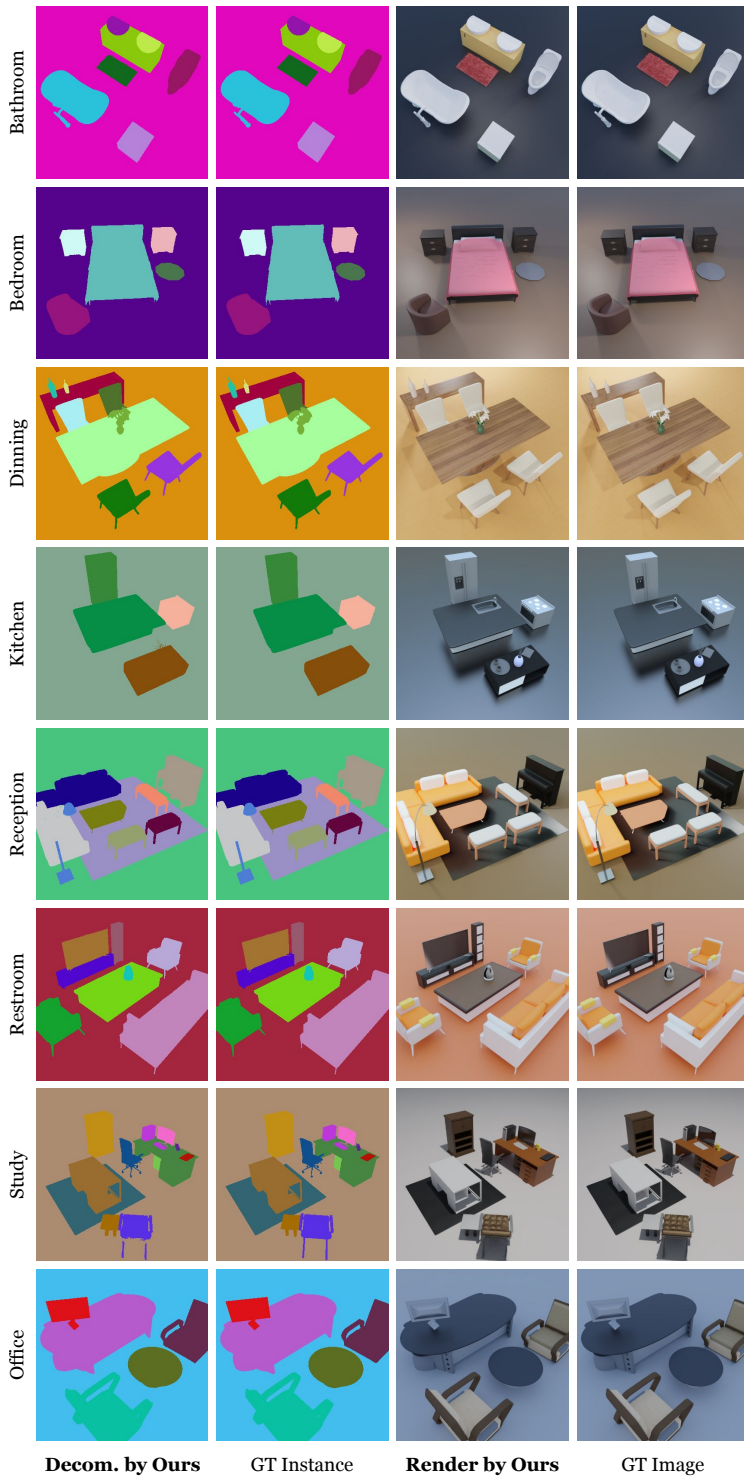


Fig. 11. Qualitative results for scene rendering and decomposition on DM-SR.

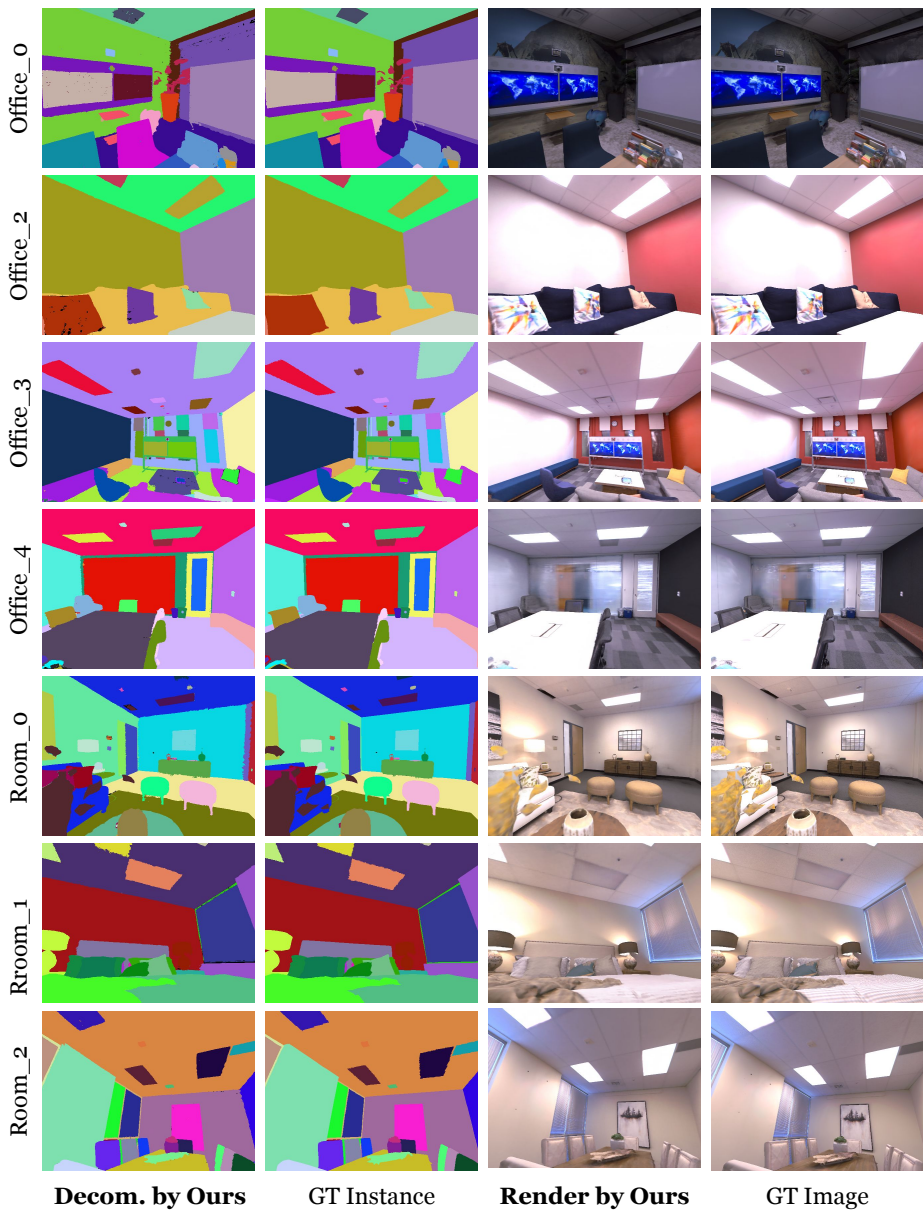


Fig. 12. Qualitative results for scene rendering and decomposition on Replica.

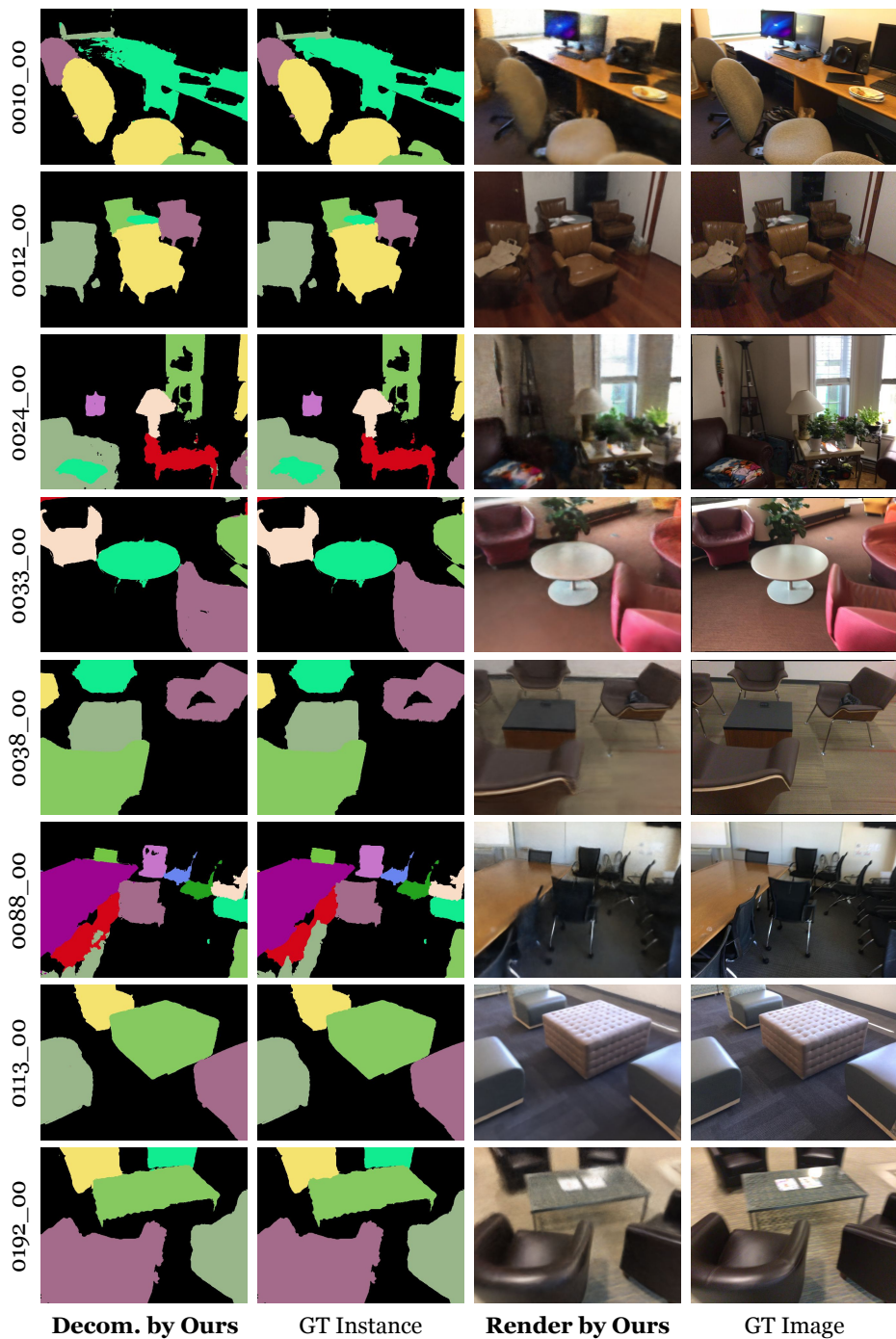
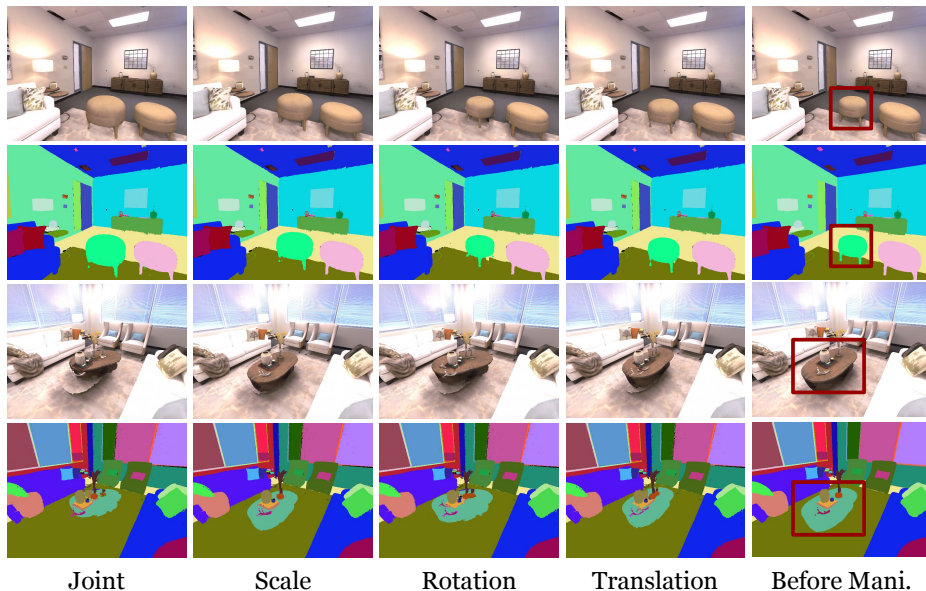
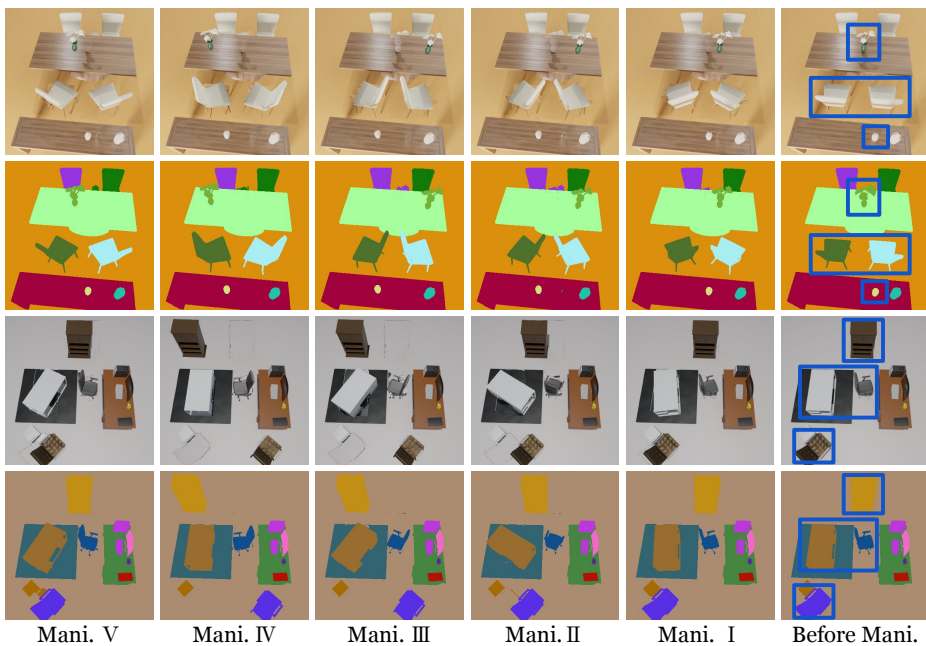


Fig. 13. Qualitative results for scene rendering and decomposition on ScanNet.



**Fig. 14.** Qualitative results for single object manipulation on Replica dataset. The dark red box in the rightmost column highlights the manipulated object.



**Fig. 15.** Qualitative results for multiple objects manipulation on DM-SR dataset. The dark blue boxes in the rightmost column highlight the manipulated objects.